

# Modeling of Anechoic Chambers With Equivalent Materials and Equivalent Sources

Silvano Chialina, Matteo Cicuttin, Lorenzo Codecasa, Giovanni Solari, Ruben Specogna, and Francesco Trevisan

**Abstract**—Numerical simulation of anechoic chambers is an important topic nowadays, since it can provide useful data about the performance of an electromagnetic compatibility site. However, the mathematical nature of the problem, the physical dimensions of the simulated sites, and the frequency ranges pose non-trivial challenges to the numerical simulation. Computational requirements, in particular, will quickly become unmanageable if adequate techniques are not employed. In this paper, we describe a novel approach, based on equivalent elements, that enables the simulation of large chambers with modest computational resources. The method is then validated against 558 real measurement results.

**Index Terms**—Anechoic chambers, computational electromagnetics, electromagnetic analysis, equivalent elements.

## I. INTRODUCTION

THE performance of an electromagnetic compatibility (EMC) site is usually validated either with experimental approaches, like [1], and numerical approaches, like [2]. Both approaches are of great importance and subject of current research; moreover, they are not exclusive but complementary because each one can confirm the validity of the other. On the numerical side, simulation of anechoic chambers is a very attractive topic since it can provide useful data about the performance of an EMC site in short times and with reduced costs. However, the mathematical properties of the underlying problem, combined with the huge physical dimensions of the typical sites, make its numerical solution very challenging.

In this paper, we describe a novel approach for the numerical simulation of entire anechoic chambers in the frequency domain. Instead of describing the geometry using a mesh with all the geometric details, we use equivalent models for the cone-ferrite assemblies and for radiating elements. This allows us to considerably reduce the number of mesh elements, and thus the computational resources required for the simulation, without degrading the accuracy of the results. In particular, our method allowed to simulate 558 different configurations of antenna positions and frequencies in a very short time on a common dual-Xeon workstation.

Manuscript received February 12, 2015; revised July 19, 2015 and January 07, 2016; accepted February 17, 2016. Date of publication April 12, 2016; date of current version July 22, 2016.

S. Chialina and G. Solari are with Emilab s.r.l., Amaro UD I-33020, Italy (e-mail: silvano.chialina@emilab.it; giovanni.solari@emilab.it).

M. Cicuttin, R. Specogna, and F. Trevisan are with the Dipartimento di Ingegneria Elettrica, Università degli Studi di Udine, Udine I-33100, Italy (e-mail: matteo.cicuttin@uniud.it; ruben.specogna@uniud.it; trevisan@uniud.it).

L. Codecasa is with the Dipartimento di Elettronica, Informazione e Bioingegneria, Politecnico di Milano, Milano I-20133, Italy (e-mail: lorenzo.codecasa@polimi.it).

Color versions of one or more of the figures in this paper are available online at <http://ieeexplore.ieee.org>.

Digital Object Identifier 10.1109/TEMC.2016.2547327

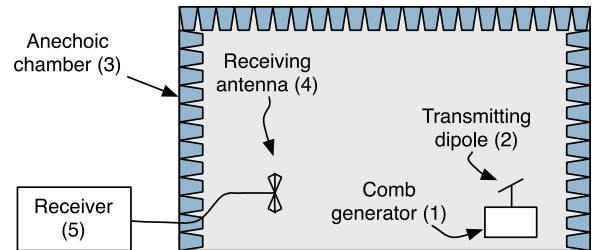


Fig. 1. Setup used to measure the field radiated by the (1) comb generator attached to the (2) test dipole within the (3) anechoic chamber containing (4) receiving antenna (4). Outside the chamber there is the (5) EMI receiver.

To validate the presented method, an experiment was devised: We set up a transmitter attached to a dipole inside a semianechoic chamber, with a measuring antenna 3 m away. We then simulated the same setup with our methodology and compared the numerical results with the real field measurements.

In the following sections, we first describe the experimental setup and then we set an *uncertainty budget* on the measurements. Then, the numerical part is presented: A brief introduction to the *discrete geometric approach (DGA)*, the numerical method employed to solve the frequency-domain wave propagation problem, is given. The technique of substituting complex radiating elements with equivalent ones, which we will refer to as *equivalent radiator method*, is then presented; theoretical aspects are discussed together with the applicability conditions of the technique. In a subsequent section, an equivalent dipole is validated by comparing the simulation with the field computed from the closed-form expression of a dipole. Finally, the modeling of the entire anechoic chamber is presented together with the comparison between the numerical results and the measurements.

## II. EXPERIMENTAL SETUP DESCRIPTION

Our experiment consisted in the measurement of the electric field produced by an RF radiator placed inside an anechoic chamber. The transmitter consisted of a comb generator connected to a specifically designed dipole. On the receiver side, a biconical antenna was attached to an EMI receiver (see Fig. 1). Transmitting and receiving antennas were placed at prescribed positions.

### A. Measurement Setup

Field measurements were made with transmitting and receiving antennas placed at heights of 1, 1.5 and 2 m both in horizontal and vertical polarization, at a distance of 3 m. It should be noted that the measurements were made at fixed positions, and

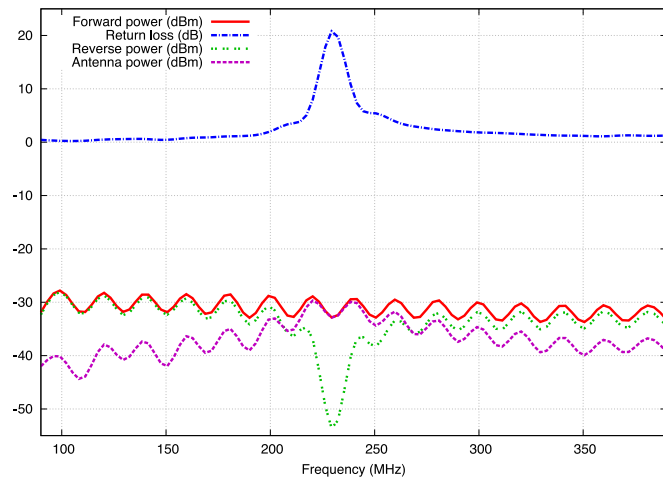


Fig. 2. Summary of the data obtained from the characterization of the comb generator and the antenna:  $P_{\text{fwd}}$ ,  $P_{\text{rev}}$ , return loss, and  $P_{\text{ant}}$ . The data are interpolated for clarity of visualization, but measurements were made at discrete steps of 10 MHz.

not by maximization as in the evaluation of the normalized site attenuation (NSA). This gave us a total of  $3 \times 3 \times 2 = 18$  different measurement setups. Measurements consisted of sweeps from 90 to 390 MHz at steps of 10 MHz. The two frequency limits were chosen mostly for practical reasons. In particular, the antennas employed in the experiments cannot perform well outside that range. On the other hand, the chosen range allowed to use the same mesh for all the frequencies.

### B. Instrumentation

The measurements involved a number of instruments, in particular:

- 1) comb generator;
- 2) Hewlett–Packard 8591EM spectrum analyzer;
- 3) Agilent 9038A EMI receiver;
- 4) ad hoc transmitting dipole;
- 5) Schwarzbeck UBAA9114 biconical antenna;
- 6) Hewlett–Packard 8753E vector network analyzer (VNA).

The performance of all instruments was perfectly known, except for the comb generator and the transmitting dipole, which required careful characterization (summarized in Fig. 2).

1) *Comb Generator*: The comb generator is a specifically designed battery-powered instrument capable to generate harmonics from 10 MHz to well above 1 GHz in steps of 10 MHz. Its power spectrum was measured to obtain, for each harmonic, the amount of *forward power*  $P_{\text{fwd}}$  supplied to the transmitting dipole. With the aid of a directional coupler, it was determined that the power spectrum of the comb generator changed by negligible amounts when changing its load. Moreover, as depicted in Fig. 2, the comb generator shows slightly different power levels for even and odd harmonics.

2) *Antenna Characterization*: The characterization of the transmitting antenna was a central topic of the proposed scheme. The complex impedance  $Z_{\text{ant}} = R_{\text{ant}} + iX_{\text{ant}}$  of the transmitting dipole was measured with the aid of the VNA. The impedance measurement was made for all the six antenna posi-

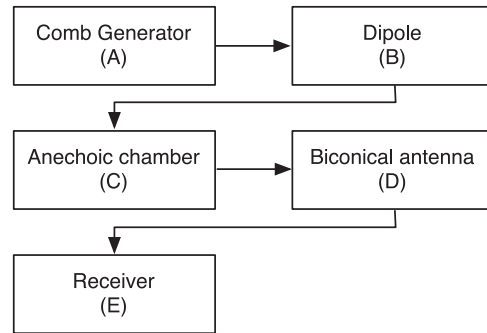


Fig. 3. Schematic representation of the components involved in the measurement chain.

tions (three heights and two polarizations). From the impedance, return loss  $RL$  was computed and used to calculate the *reverse power*  $P_{\text{rev}}$  flowing from the antenna back to the comb generator because of the mismatch. As a cross check, the dipole was simulated with NEC2 code, which confirmed the measurements. The indirect measurement of  $P_{\text{rev}}$  subsequently allowed to compute the *net power*  $P_{\text{ant}}$  with a good accuracy, despite of the heavy mismatch between the generator and the antenna. Finally, using  $P_{\text{ant}}$  and the antenna impedance, the supply current at the feedpoint of the dipole was computed as

$$I_0 = \sqrt{\frac{P_{\text{ant}}}{R_{\text{ant}}}}. \quad (1)$$

The knowledge of  $I_0$  will be needed in the numerical part of this paper, as an input for the simulation.

### C. Measurement Chain Uncertainty Calculation

To define a mathematical model of the measurement process, the entire measurement chain can be schematically illustrated as in Fig. 3. From the already mentioned comb generator, marked as (A), the signal goes to the dipole (B), which radiates the electromagnetic field in the semianechoic chamber (C). The semi-anechoic chamber is an EMC site that mimics the *Open Area Test Site*, whose primary characteristic is a metallic ground plane which behaves as a reflective surface. The mirror effect implies that on the receiving antenna, the signal is the sum of a direct wave and a reflected wave which, in turn, produces different signal levels at different receiving antenna positions. Moreover, in a real anechoic chamber, there are multiple secondary signal paths due to the reflections on the walls and on the ceiling. These effects are considered as site imperfections and are taken into account in the NSA, a parameter measured using standard procedures [9]. Because of these effects, the field measurement at fixed positions, as we made in our experiments, is particularly challenging. At the chosen measurement points, the signal is received with a biconical antenna (D) and transferred to the receiver (E), which gives the experimental reading. Each block depicted in Fig. 3 contributes to the measurement uncertainty, in particular the measured amplitude of the electric field  $|e_m|$

$$|e_m| = \sum_i x_i \quad (2)$$

TABLE I  
SUMMARY OF THE UNCERTAINTY CONTRIBUTES  $x_i$  IN THE MEASUREMENTS

Symbol ( $x_i$ )	Meaning	Uncertainty	Probability distribution	Normalization factor	$u_i(x_i)$	$c_i$	$c_i u_i(x_i)$
$R_i$	Receiver reading	0.1	normal 1	1.00	0.10	1.00	0.10
$L_{ar}$	Receiver-antenna cable attenuation	0.2	normal 2	2.00	0.10	1.00	0.10
$AF$	UBAA9114 antenna factor	0.5	normal 2	2.00	0.25	1.00	0.25
Receiver Corrections							
$V_{sw}$	Sine wave voltage	0.4	normal 2	2.00	0.20	1.00	0.20
$L_{mar}$	Antenna-receiver mismatch	0.1	U-shape	1.41	0.07	1.00	0.07
Biconical antenna corrections							
$AF_i$	AF frequency interpolation	0.3	rectangular	1.73	0.17	1.00	0.17
$AF_h$	AF height deviation	1.5	rectangular	1.73	0.87	1.00	0.87
$AF_{dir}$	Directivity difference	0.5	rectangular	1.73	0.29	1.00	0.29
Site corrections							
$dSA$	Site imperfections (max)	3.0	triangular	2.45	1.22	1.00	1.22
$dH$	Table height	0.1	rectangular	2.00	0.05	1.00	0.05
$Rr$	Repeatability	0.5	normal 1	1.00	0.50	1.00	0.50
Transmitter corrections							
$TXi$	Comb level	0.5	rectangular	1.73	0.29	1.00	0.29
$dMta$	Mismatch: antenna-comb generator	0.24	U-shape	1.41	0.17	1.00	0.17
$Gtx$	TX antenna gain	2.0	rectangular	1.73	1.15	1.00	1.15
$u_t$	Total uncertainty ( $\sqrt{\sum_i (c_i u(x_i))^2}$ )						2.03
$u_e$	Expanded uncertainty ( $k = 2$ ) [dB]						4.05

is given by the sum of the factors  $x_i$  expressed in logarithmic scale, which are reported in Table I. While some of them have a quite intuitive meaning (reported in Table I), others deserve special attention, in particular:

- 1) uncertainty on antenna factor  $AF$ : Since the  $AF$  is measured on a discrete set of frequencies, there is an error due to interpolation, denoted as  $AF_i$ . Moreover, the antenna factor changes with antenna height and antenna axis direction, these effects are denoted by  $AF_h$  and  $AF_{dir}$ ;
- 2) site imperfections  $dSA$ : The site imperfections are accounted for by the  $NSA$  [9].

Moreover, some other important parameters were set to zero and, thus, omitted from Table I, in particular:

- 1) noise floor  $V_{nf}$ : The uncertainty due to the noise floor was considered negligible since all the measurements had an adequate signal-to-noise ratio ( $> 10$  dB);
- 2) cross polarization  $A_{cp}$  and unbalance  $A_{bal}$ : These two contributes are set to zero because of antenna specifications.

Once all the factors and their uncertainties are known, the total uncertainty  $u_t$  and the extended uncertainty  $u_e = 2u_t$  are calculated as [10]

$$u_t = \sqrt{\sum_i [c_i u(x_i)]^2} \quad (3)$$

where  $c_i$  is the sensitivity coefficient of the  $i$ th contribute  $x_i$ , while  $u_i(x_i)$  is its uncertainty value. The sensitivity coefficient is calculated as [10]

$$c_i = \frac{\partial |e_m|}{\partial x_i} \quad (4)$$

### III. OVERVIEW

#### A. Electromagnetic Problem

The electromagnetic wave propagation problem in the frequency domain at angular frequency  $\omega$  is written as

$$\nabla \times (\boldsymbol{\nu} \nabla \times \mathbf{e}) - \omega^2 \boldsymbol{\epsilon} \mathbf{e} = \mathbf{0} \quad (5)$$

where  $\mathbf{e}$  is a complex-valued vector function of the position, representing the electric field, while  $\boldsymbol{\epsilon}$  and  $\boldsymbol{\nu}$  are, respectively, the electric and the magnetic material positive definite tensors. Problem (5) can be solved subject to specific boundary conditions, for example, the admittance boundary condition

$$\mathbf{h} \times \mathbf{n} = Y((\mathbf{n} \times \mathbf{e}) \times \mathbf{n}) \quad (6)$$

where  $Y = 1/Z$ . Admittance is used since it arises naturally from the discrete formulation [3].

#### B. DGA Formulation of the Electromagnetic Problem

The DGA requires a discretization of the region  $\Omega$  in which the problem is defined, consisting a pair of interlocked grids  $\mathcal{G}$  and  $\tilde{\mathcal{G}}$ .  $\mathcal{G}$  is a tetrahedral grid, while  $\tilde{\mathcal{G}}$  is obtained from  $\mathcal{G}$  by barycentric subdivision [3]. The electromagnetic quantities are defined on the geometric elements composing these grids, in particular

- 1) the electromotive force  $U_i = \int_{e_i} \mathbf{e} \cdot d\mathbf{l}$  on the primal edges  $e_i \in \mathcal{G}$ ;
- 2) the magnetic flux  $\Phi_i = \int_{f_i} \mathbf{b} \cdot d\mathbf{s}$  on the primal faces  $f_i \in \mathcal{G}$ ;
- 3) the magnetomotive force  $F_i = \int_{\tilde{e}_i} \mathbf{h} \cdot d\mathbf{l}$ , on the dual edges  $\tilde{e}_i \in \tilde{\mathcal{G}}$ ;
- 4) the electric flux  $\Psi_i = \int_{\tilde{f}_i} \mathbf{d} \cdot d\mathbf{s}$ , on the dual faces  $\tilde{f}_i \in \tilde{\mathcal{G}}$ .

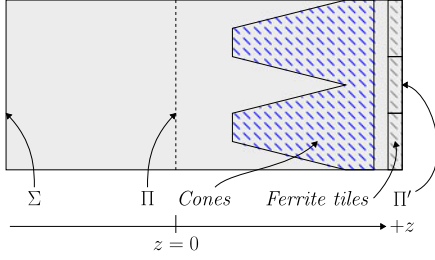


Fig. 4. Cross section of the unit cell, showing pyramidal absorbers (cones) and ferrite tiles. Solid gray regions represent air.

Moreover, the standard face-edge incidence matrices  $\mathbf{C}$  on  $\mathcal{G}$  and  $\mathbf{C}^T$  on  $\tilde{\mathcal{G}}$  are introduced [3]. According to the DGA, the electromagnetic propagation problem (5) is written as

$$(\mathbf{C}^T \mathbf{M}_\nu \mathbf{C} - \omega^2 \mathbf{M}_\epsilon) \mathbf{U} = \mathbf{0} \quad (7)$$

where  $\mathbf{U}$  is an array collecting circulations of the electric field on primal edges, while symmetric positive definite material matrices  $\mathbf{M}_\epsilon$  and  $\mathbf{M}_\nu$  are calculated according to [5].

### C. Impedance Boundary Condition

The discrete counterpart of the admittance boundary condition (6) is encoded as

$$\mathbf{F}^b = \mathbf{M}_Y \mathbf{U} \quad (8)$$

where the array  $\mathbf{F}^b$  has the same number of elements of  $\mathbf{U}$ , but its nonzero entries are only the ones associated to dual boundary edges  $\tilde{e}_b$  of  $\partial\Omega$  [3], which are in one to one correspondence to primal boundary edges  $e_b$ .

The matrix  $\mathbf{M}_Y$  has also nonzero entries only in correspondence of the boundary edges. Its entries are calculated from the admittance parameter  $Y$ . According to Codecasa *et al.* [3], condition (8) is integrated into (7) as

$$(\mathbf{C}^T \mathbf{M}_\nu \mathbf{C} - \omega^2 \mathbf{M}_\epsilon) \mathbf{U} + i\omega \mathbf{M}_Y \mathbf{U} = \mathbf{0}. \quad (9)$$

### D. Plane Wave Excitation

The impedance boundary condition can be extended to represent a plane wave excitation [4], which is encoded in the right side of (9) as

$$(\mathbf{C}^T \mathbf{M}_\nu \mathbf{C} - \omega^2 \mathbf{M}_\epsilon) \mathbf{U} + i\omega \mathbf{M}_Y \mathbf{U} = -2i\omega \mathbf{F}^{b^-} \quad (10)$$

where  $\mathbf{F}^{b^-}$  is nonzero only in correspondence of the edges of the boundary, where the plane wave is forced and collects the magnetomotive forces due to the excitation.

### E. Unit Cell Model

All the ideas exposed so far can be used to study the basic element of an anechoic wall, which we call *unit cell* [4]. A unit cell is a section of an anechoic wall composed by  $2 \times 2$  absorbing cones and  $3 \times 3$  ferrite tiles. In front of the cones and between the cones and the ferrite tiles there is air, as detailed in Fig. 4.

The goal of studying the unit cell is to obtain an equivalent representation [4] in terms of an admittance boundary condition. This is done by the following steps:

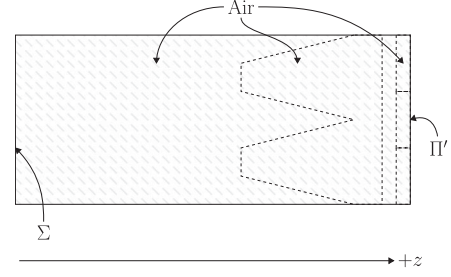


Fig. 5. Cross section of the unit cell, with pyramidal absorbers and ferrite tiles removed (dashed lines are for reference). All the regions previously filled with absorbing material are now empty space filled with air.

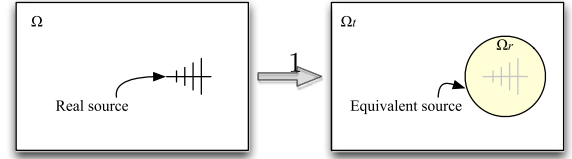


Fig. 6. Real source (left) is transformed in an empty sphere (right). Because the field of the original source is projected onto the surface of the sphere, it radiates a field equivalent to the original one.

- 1) Apply a plane wave excitation on the plane  $\Sigma$ .
- 2) Calculate wave impedance on the plane  $\Pi$ .
- 3) Remove all the materials inside the unit cell and translate the impedance calculated on  $\Pi$  to  $\Pi'$  (Fig. 5).
- 4) Use the translated impedance as impedance boundary condition for entire walls in the simulation of the entire anechoic chamber.

## IV. EQUIVALENT RADIATING ELEMENTS

In this section, it will be shown that how a generic radiating element, for example, an antenna, can be substituted by an equivalent model. The idea is to substitute an arbitrarily complex object with a sphere radiating a field with the same characteristics of the original one. To achieve this goal, the domain  $\Omega$  is partitioned in two regions  $\Omega_S$  and  $\Omega_T$ .

The region  $\Omega_S$  is the one that contains the radiator, while the region  $\Omega_T$  is the remaining part. Moreover, in the region  $\Omega_T$ , the *total field* is calculated, while in the region  $\Omega_S$ , only the *scattering field* is computed (see Fig. 6). In this way, it is possible to evaluate the reaction of the environment to the field radiated by the radiator itself. The separation of  $\Omega_T$  and  $\Omega_S$  is obtained by introducing a *boundary dual grid*, whose role is to adjust the discrete Maxwell's equations on the interface  $\Sigma$  between the two regions  $\Omega_T$  and  $\Omega_S$ . The adjustment consists of projecting on  $\Sigma$  the fields due to the radiation of the original source: in the following sections, it will be shown how this can be done *locally* (i.e., element wise). Global equations are then obtained by *assembling* the local contributes in the usual way. In the following discussion, local quantities will be denoted with the superscript  $v$ , except for the matrix  $\mathbf{C}$ , which we assume the local one unless otherwise noted. Moreover, we choose that the edges of  $\Sigma$  belong to  $\Omega_S$ . This means that tetrahedra in  $\Omega_S$  and touching  $\Sigma$  are the only affected by the modified Maxwell

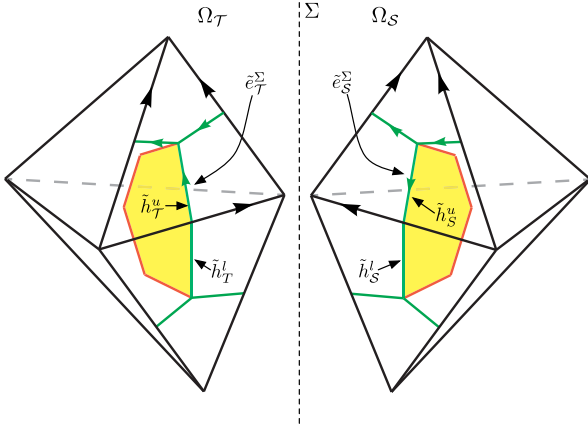


Fig. 7. Cluster of tetrahedra having  $\Sigma$  in common where *boundary dual edges* are shown. Since half-dual edges  $\tilde{h}_T^u$  and  $\tilde{h}_S^u$  are the same edge but with opposite orientation, the associated magnetomotive forces  $F_T$  and  $F_S$  sum to zero. But since  $F_S = F_{S_s} + F_{S_r}$ , also  $F_T + F_{S_s} = -F_{S_r}$  holds.

equations shown below. Every other tetrahedra in  $\Omega$  is treated as usual.

#### A. Ampère–Maxwell Law

Consider, in relation to Fig. 7, the boundary dual edges  $\tilde{e}_T^\Sigma$  and  $\tilde{e}_S^\Sigma$ , each spanning two tetrahedra. Both  $\tilde{e}_T^\Sigma$  and  $\tilde{e}_S^\Sigma$  can be split in two parts, which we call *half edges*, such that  $\tilde{e}_T^\Sigma = \tilde{h}_T^u \cup \tilde{h}_T^l$  and  $\tilde{e}_S^\Sigma = \tilde{h}_S^u \cup \tilde{h}_S^l$ . Each half edge belongs to a single tetrahedron, for example,  $\tilde{h}_T^u$  belongs to the upper tetrahedron in  $\Omega_T$ , while  $\tilde{h}_S^l$  belongs to the lower tetrahedron in  $\Omega_S$  (see Fig. 7). To write the contribute to the Ampère–Maxwell law for the single tetrahedron  $v$ , only the half edges belonging to  $v$  must be considered. Reasoning on the two upper tetrahedra in Fig. 7, Ampère–Maxwell law is obtained by observing that the magnetomotive force  $F_T$  on  $\tilde{h}_T^u$  and  $F_S$  on  $\tilde{h}_S^u$  must satisfy the relation  $F_T^\Sigma + F_S^\Sigma = 0$  because  $\tilde{h}_T^u$  and  $\tilde{h}_S^u$  are in fact the same edge but with opposite orientation. However, since we impose the excitation on the scattering subdomain, the magnetomotive force  $F_S$  can be further decomposed in the unknown scattered contribute  $F_{S_s}$  and in the known radiated contribute  $F_{S_r}$ . This implies that the balance of the magnetomotive forces must satisfy the condition  $F_T + F_{S_s} = -F_{S_r}$ . Thus, the local Ampère–Maxwell law for a tetrahedron  $v$  in  $\Omega_S$  touching  $\Sigma$  is written as

$$\mathbf{C}^T \mathbf{F}^v - \mathbf{F}_r^v = i\omega \Psi^v \quad (11)$$

where the term  $\mathbf{F}_r^v$  collects the magnetomotive forces on the half edges of  $v$  due to the excitation.

#### B. Faraday–Neumann Law

To derive the expression for the Faraday–Neumann law, tetrahedra on the interface  $\Sigma$  must be studied. In particular, two cases are identified:

- 1) volume element with an edge lying on  $\Sigma$ ;
- 2) volume element with a face lying on  $\Sigma$ .

1) *The Case of a Face on  $\Sigma$* : Consider a volume element  $v$  lying on  $\Sigma$ , the faces of which are  $f_1, \dots, f_4$  and their magnetic fluxes are collected in the array  $\Phi^v = (\phi_1^v, \dots, \phi_4^v)$ . Assume,

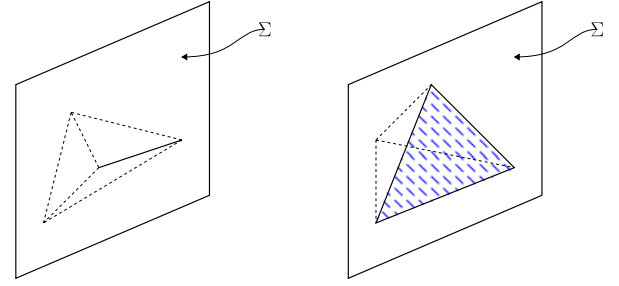


Fig. 8. Two cases of interest of elements touching  $\Sigma$ : the *edge case* on the left side and the *face case* on the right side.

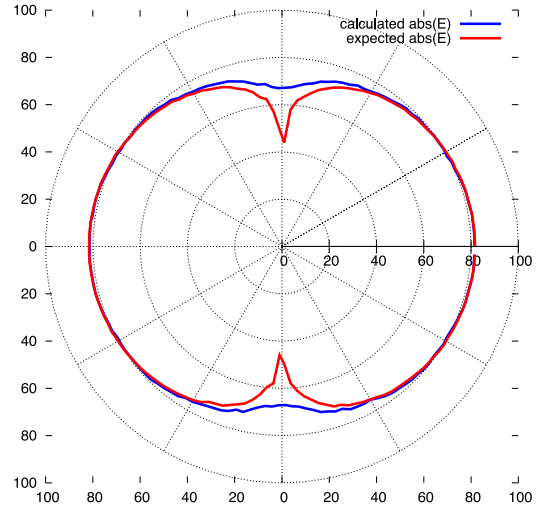


Fig. 9. Comparison between the expected field and the field produced by the equivalent model at  $f = 230$  MHz. The field is expressed in  $\text{dB}\mu\text{V/m}$ .

without loss of generality, that the face on  $\Sigma$  is  $f_1$ , so  $v \cap \Sigma = f_1$  (see Fig. 8). Assume also that the edges surrounding  $f_1$  are  $e_1, e_2, e_3$ . Both electromotive forces  $U_1^v, U_2^v, U_3^v$  and flux  $\phi_1^v$  on  $f_1$  can be decomposed in an unknown scattering component and in a known radiated component, obtaining  $U_k^v = U_{k,s}^v + U_{k,r}^v$  with  $k \in \{1, 2, 3\}$  and  $\phi_1^v = \phi_{1s}^v + \phi_{1r}^v$ . In this case, both sides of the Faraday–Neumann law are modified, as follows:

$$\mathbf{C} \begin{pmatrix} U_{1s}^v + U_{1r}^v \\ U_{2s}^v + U_{2r}^v \\ U_{3s}^v + U_{3r}^v \\ U_4^v \\ U_5^v \\ U_6^v \end{pmatrix} = -i\omega \begin{pmatrix} \phi_{1s}^v + \phi_{1r}^v \\ \phi_2^v \\ \phi_3^v \\ \phi_4^v \end{pmatrix}. \quad (12)$$

Separating known and unknown quantities and writing the equation in compact form, we obtain

$$\mathbf{C} (\mathbf{U}_r^v + \mathbf{U}_s^v) = -i\omega (\Phi_r^v + \Phi_s^v). \quad (13)$$

2) *Case of an Edge on  $\Sigma$* : In this case, (13) remains valid by setting to zero the radiated contributes of the geometric elements not touching  $\Sigma$  (see Fig. 8).

### C. Constitutive Relations

Almost the same reasoning carried out for the Faraday–Neumann law must be made for the constitutive relations when dealing with volume elements lying on  $\Sigma$ . There are again two cases, the one of the edge on  $\Sigma$ , and the one of the face on  $\Sigma$ .

1) *Case of a Face on  $\Sigma$* : In this case, both electromotive forces and magnetic fluxes are split in radiated and scattered contributes, obtaining

$$\Psi^v = \mathbf{M}_\epsilon^v \begin{pmatrix} U_{1s}^v + U_{1r}^v \\ U_{2s}^v + U_{2r}^v \\ U_{3s}^v + U_{3r}^v \\ U_4^v \\ U_5^v \\ U_6^v \end{pmatrix} = \mathbf{M}_\epsilon^v \begin{pmatrix} U_{1s}^v \\ U_{2s}^v \\ U_{3s}^v \\ U_4^v \\ U_5^v \\ U_6^v \end{pmatrix} + \mathbf{M}_\epsilon^v \begin{pmatrix} U_{1r}^v \\ U_{2r}^v \\ U_{3r}^v \\ 0 \\ 0 \\ 0 \end{pmatrix} \quad (14)$$

$$\mathbf{F}^v = \mathbf{M}_\nu^v \begin{pmatrix} \phi_{1s}^v + \phi_{1r}^v \\ \phi_2^v \\ \phi_3^v \\ \phi_4^v \end{pmatrix} = \mathbf{M}_\nu^v \begin{pmatrix} \phi_{1s}^v \\ \phi_2^v \\ \phi_3^v \\ \phi_4^v \end{pmatrix} + \mathbf{M}_\nu^v \begin{pmatrix} \phi_{1r}^v \\ 0 \\ 0 \\ 0 \end{pmatrix} \quad (15)$$

or, written in compact form,

$$\Psi^v = \mathbf{M}_\epsilon^v (\mathbf{U}_s^v + \mathbf{U}_r^v) \quad (16)$$

$$\mathbf{F}^v = \mathbf{M}_\nu^v (\Phi_s^v + \Phi_r^v). \quad (17)$$

2) *Case of an Edge on  $\Sigma$* : As in the case of the Faraday–Neumann law, in this case there are no magnetic fluxes across  $\Sigma$  and only one voltage along an edge on  $\Sigma$ . Constitutive relations (16) and (17) continue to remain valid by setting to zero the radiated contribute of the entries corresponding to geometric entities not on  $\Sigma$  (see Fig. 8).

### D. From Local Equations to the Global Equation

Until now, we reasoned in terms of single mesh volumes, so an assembly phase must be carried out in order to obtain the global equation. Consider (11), (13), (16), and (17), by solving (11) for  $(\Phi_r^v + \Phi_s^v)$  then substituting (11), (16), (17) and rearranging, the expression

$$\mathbf{K}^v \mathbf{U}_s^v = -\mathbf{K}^v \mathbf{U}_r^v - i\omega \mathbf{F}_r^v \quad (18)$$

is obtained, where  $\mathbf{K}^v = \mathbf{C}^T \mathbf{M}_\nu^v \mathbf{C} - \omega^2 \mathbf{M}_\epsilon^v$ . Assembling element by element in the usual way, the equation

$$\mathbf{K} \mathbf{U} = -\mathbf{K} \mathbf{U}_r - i\omega \mathbf{F}_r \quad (19)$$

is obtained, where all the matrices involved are *global*. The unknowns  $\mathbf{U}_s^v$  from (18) are now a part of the unknown  $\mathbf{U}$  in (19) and appear in the positions corresponding to the primal edges of  $\Sigma$ . Moreover, the terms  $\mathbf{U}_r$  and  $\mathbf{F}_r$  are nonzero only in correspondence of the primal edges of  $\Sigma$  and the dual edges of  $\Sigma$ , respectively. By introducing the terms due to the impedance boundary conditions (9) and plane wave excitation (10), the full equation is obtained

$$\mathbf{K} \mathbf{U} + i\omega \mathbf{M}_Y \mathbf{U} = -\mathbf{K} \mathbf{U}_r - i\omega \mathbf{F}_r - 2i\omega \mathbf{F}^{b-}. \quad (20)$$

### E. Equivalent Antenna

Given an antenna of arbitrary shape, radiated electric and magnetic fields can be computed in each point of space by means of tools like NEC or other, more advanced, simulators. In our case, we used a dipole, for which the radiated electromagnetic field is known in closed form [6]:

$$E_\theta = \frac{i\eta I_0 e^{-ikr}}{2\pi r} \left[ \frac{\cos\left(\frac{kL}{2} \cos\theta\right) - \cos\left(\frac{kL}{2}\right)}{\sin\theta} \right] \quad (21)$$

$$H_\phi = \frac{E_\theta}{\eta} \quad (22)$$

where  $\eta$  is the impedance of free space,  $I_0$  is the excitation current at the feedpoint (1),  $k$  is the propagation constant,  $L$  is the dipole length, and  $r$  is the distance. In (21) and (22), it is assumed that the dipole lies along the  $z$ -axis of a cartesian reference system and its center is in the origin. On our simulator, arbitrary rotations of the virtual dipole are obtained by means of quaternions [7]. Once the field is known, it can be used to compute the values of the electromotive forces across the primal edges of the interface  $\Sigma$  and the magnetomotive forces across its dual edges.

## V. VALIDATION OF THE EQUIVALENT MODEL

The diameter of the sphere representing the equivalent radiator and the average edge length of tetrahedra in its surroundings must be properly tuned, according to the operating frequency. To obtain reasonable performance, the diameter should be comparable with the wavelength  $\lambda$  and the edge length should be comparable with  $\lambda/10$ . However, these are only rough indications; in our experiments, a single mesh tuned for the center frequency proved to be adequate between  $\lambda = 3.3$  m and  $\lambda = 0.77$  m. To validate the equivalent model, a cube of side  $l = 5$  m was considered, while the radiator was represented by a sphere of radius  $r = 0.75$  m placed in the center of the cube. The boundary conditions on the six faces of the cube were set to *impedance boundary condition* [3] with  $Z = \sqrt{\mu_0/\epsilon_0}$ . Electromagnetic wave propagation problem was solved and the field was evaluated at  $r = 2.5$  m (Fig. 9).

## VI. MODELING OF AN ANECHOIC CHAMBER

Using the results developed in this paper and in [4], an entire anechoic chamber with a transmitter inside was simulated. The chamber, located at the Emilab EMC laboratory and manufactured by ETS-Lindgren, has dimensions (in  $x$ ,  $y$  and  $z$ ) of  $8.64$  m  $\times$   $5.6$  m  $\times$   $5.68$  m.

### A. Anechoic Chamber Walls

The walls of the anechoic chamber were transformed to equivalent surfaces and treated as impedance boundary conditions using the methodology described in our previous work [4]. This step was done frequency by frequency and required 31 simulations. Cone and ferrite material parameters were provided by the manufacturer as tables of complex values of  $\epsilon_r$  and  $\mu_r$ , in steps of 4 MHz. For the frequencies where tabulated data were not available, linear interpolation was used to calculate the value.

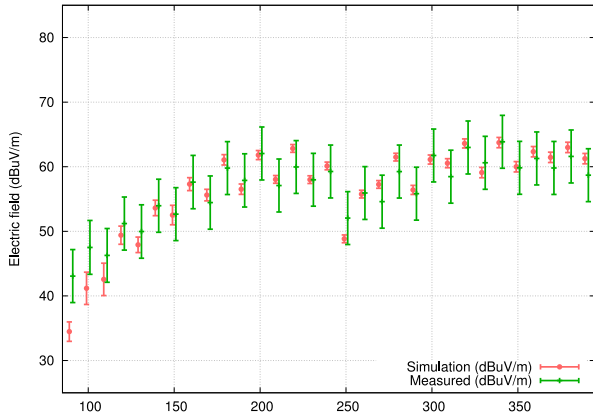


Fig. 10. Comparison between simulation and measurements. Setup: TX at 1.5 m, RX at 1.5 m, horizontal polarization.

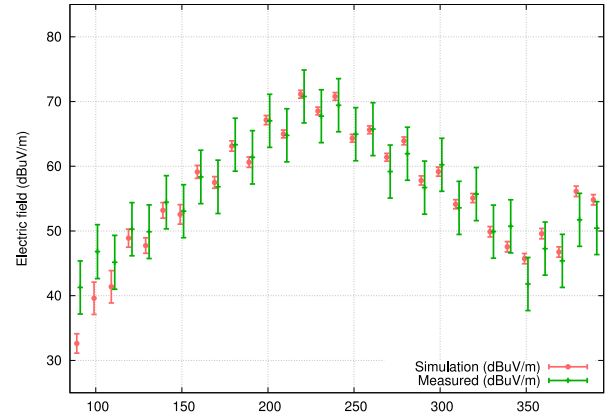


Fig. 11. Comparison between simulation and measurements. Setup: TX at 1.5 m, RX at 1 m, horizontal polarization.

## B. Transmitter

The transmitter was simulated by means of an equivalent radiator, modeled as a sphere meeting the requirements described in Section V and with a diameter of  $r = 0.75$  m.

## VII. RESULTS

### A. Numerical Experiments

The numerical simulations were made with the EMT code, our DGA workbench written in C++11. The first step was to calculate, for each frequency, the equivalent impedance parameters for the anechoic walls using the technique of Chialina *et al.* [4]. Once the parameters were obtained, the entire anechoic chamber was described with a mesh of about 1.1 million elements. The simulations were performed on Debian/GNU Linux with kernel 3.14 running on a dual Xeon E5420 workstation with 32 GB of RAM, GCC 4.9.1 compiler, and MKL PARDISO solver. The frequency sweep from 90 to 390 MHz for each antenna configuration required running a total of  $31 \times 18 = 558$  simulations, which required slightly more than three days of runtime. A direct solver was employed, but we are investigating alternative solution techniques as multigrid.

### B. Comparison

From the comparison between experiments and simulations, we observed that our model is of remarkable accuracy. Figs. 10–15 contain the results of six of the 18 experiments we made. In almost all cases, the simulation result (dot in the left bar at each frequency) lies within the uncertainty band associated to the field measurements (right bar at each frequency). There are, however, some points where simulations and measurements do not agree.

### C. On the Discrepancies Between Simulations and Measurements

In Figs. 10–15, some simulation results fall outside the uncertainty band of the field measurement. However, until now, the antenna current used as input of the simulation was considered exact. But, as a measured quantity, the current has also an asso-

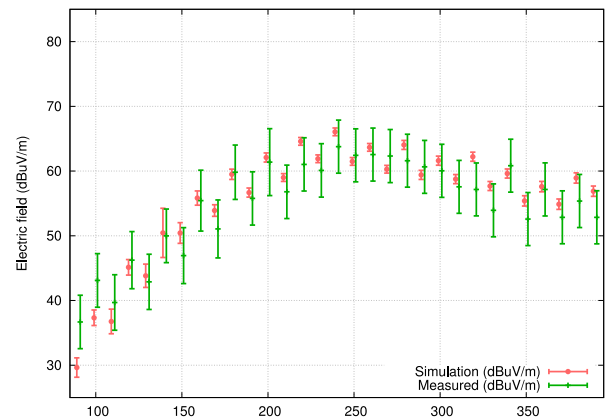


Fig. 12. Comparison between simulation and measurements. Setup: TX at 2 m, RX at 2 m, vertical polarization.

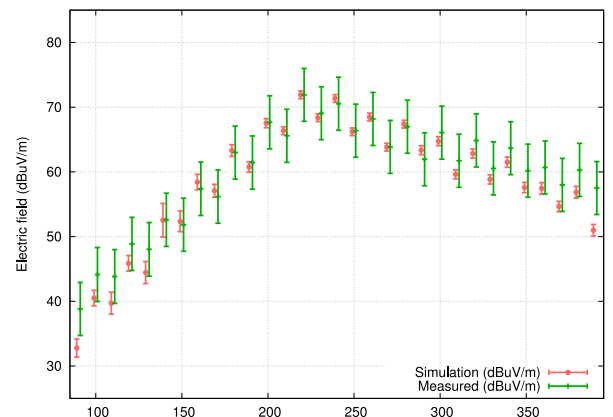


Fig. 13. Comparison between simulation and measurements. Setup: TX at 1 m, RX at 1 m, horizontal polarization.

ciated uncertainty which affects the result of the simulation. In the following, we give an estimate of that uncertainty.

The electric field radiated by the dipole, calculated as in (21), can be rewritten in logarithmic form as

$$E_{\theta, \text{dB}} = 20 \log(I_0) + 20 \log(T) \quad (23)$$

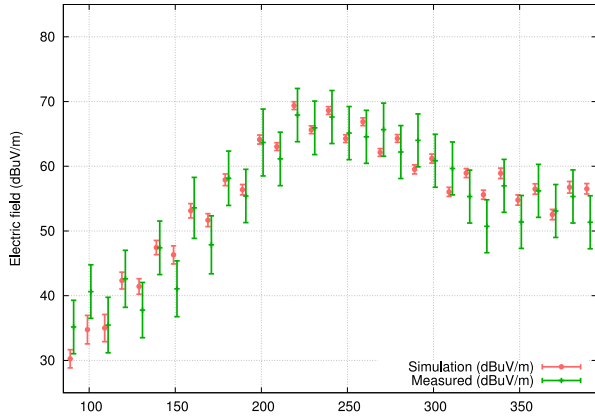


Fig. 14. Comparison between simulation and measurements. Setup: TX at 1.5 m, RX at 1.5 m, horizontal polarization.

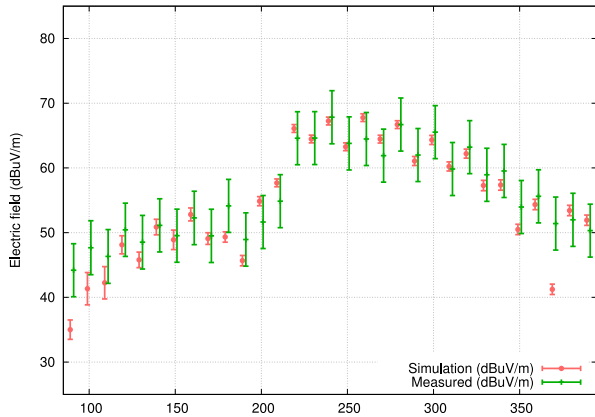


Fig. 15. Comparison between simulation and measurements. Setup: TX at 1.5 m, RX at 1.5 m, horizontal polarization.

where  $T$  accounts for all the multiplicative terms in (21). Moreover, as already detailed, the current  $I_0$  is calculated as

$$I_0 = \sqrt{\frac{P_{\text{fwd}} - P_{\text{rev}}}{Z_{\text{ant}}}} \quad (24)$$

where

$$Z_{\text{ant}} = Z_0 \frac{1 + \Gamma}{1 - \Gamma} \quad (25)$$

with  $\Gamma$  denoting the reflection coefficient. Therefore, using (24) and (25), the antenna current can be written as

$$20 \log(I_0) = 10 \log(P_{\text{fwd}}) + 20 \log(1 - \Gamma) - 10 \log(Z_0).$$

The sensitivity coefficients can now be calculated [9], [10] as

$$c_{\Gamma} = \frac{\partial(20 \log I_0)}{\partial \Gamma} = -\frac{20}{1 - \Gamma} \quad (26)$$

$$c_p = \frac{\partial(20 \log I_0)}{\partial P_{\text{fwd}, \text{dB}}} = 1. \quad (27)$$

With these coefficients, the uncertainty of the radiated field can be calculated as

$$u(E_{\theta, \text{dB}}) = c_p u_p + c_{\Gamma} u_{\Gamma} \quad (28)$$

where  $u_p$  and  $u_{\Gamma}$  have the values 0.5 and 0.01, respectively, and are derived from the instrument specifications. These considerations on the uncertainty of the input current give rise to a directly correlated uncertainty in the simulation output, depicted in Figs. 10–15.

As expected, at frequencies where the mismatch between the dipole and the source is very high (dipole resonant frequency is 230 MHz), the uncertainty is also high because  $P_{\text{fwd}}$  and  $P_{\text{rev}}$  are of comparable magnitude. In most of the cases, the discrepancy between simulations and measurements can be explained by the uncertainty on the input.

## VIII. CONCLUSION

Nowadays, numerical simulation of anechoic chambers is a central tool in the study of their performance [2], [8]. However, the mathematical nature of the problem, the physical dimensions of the simulated sites, and the frequency ranges pose nontrivial challenges to the numerical treatment of the simulation problem. In this paper, we introduced a technique to describe anechoic walls and radiating elements as equivalent models, in order to reduce the degrees of freedom of the numerical problem and, thus, the required computational resources. Since important approximations were introduced, the validity of our equivalent models was tested against 558 real measurements of which only a subset of them is included for space reasons. In general, we found a good agreement between the simulations and the measured data. The result is particularly significant since measurements were made on fixed points, and not by taking the maximum value as in the estimation of the NSA parameter.

## REFERENCES

- [1] C. F. M. Carobbi, A. Bonci, M. Cati, C. Panconi, M. Borsero, and G. Vizio, "Design, preparation, conduct, and result of a proficiency test of radiated emission measurements," *IEEE Trans. Electromagn. Compat.*, vol. 56, no. 6, pp. 1251–1261, Dec. 2014.
- [2] I. Munteanu and R. Kakerow, "Simulation methodology for the assessment of field uniformity in a large anechoic chamber," *IEEE Trans. Magn.*, vol. 50, no. 2, Feb. 2014, Art. no. 7005104.
- [3] L. Codecasa, R. Specogna, and F. Trevisan, "Discrete geometric formulation of admittance boundary conditions for frequency domain problems over tetrahedral dual grids," *IEEE Trans. Antennas Propag.*, vol. 60, no. 8, pp. 3998–4002, Aug. 2012.
- [4] S. Chialina, M. Cicuttin, L. Codecasa, R. Specogna, and F. Trevisan, "Plane wave excitation for frequency domain problems by means of impedance boundary conditions," *IEEE Trans. Magn.*, vol. 51, no. 3, Mar. 2015, Art. no. 7203504.
- [5] L. Codecasa, R. Specogna, and F. Trevisan, "Symmetric positive-definite constitutive matrices for discrete eddy-current problems," *IEEE Trans. Magn.*, vol. 43, no. 2, pp. 510–515, Feb. 2007.
- [6] C. A. Balanis, *Antenna Theory*, 3rd ed. Hoboken, NJ, USA: Wiley, 2005.
- [7] John Vince, *Quaternions for Computer Graphics*. London, U.K.: Springer-Verlag, 2011.
- [8] C. Jiakui and W. Yinghong, "Simulation of the field uniformity of anechoic chamber," in *Proc. Int. Symp. Microw., Antenna, Propag. EMC Technol. Wireless Commun.* Aug. 2007, pp. 1349–1352.
- [9] (2014). CISPR 16, Part 4-2: Uncertainties, statistics and limit modelling—Uncertainty in EMC measurements.
- [10] Joint Committee for Guides in Metrology, *JCGM 100: Evaluation of Measurement Data—Guide to the Expression of Uncertainty in Measurement*, JCGM, 2008.